

Size-dependence of the photothermal response of a single metal nanosphere

Cite as: J. Appl. Phys. **126**, 173103 (2019); <https://doi.org/10.1063/1.5123629>

Submitted: 07 August 2019 . Accepted: 14 October 2019 . Published Online: 04 November 2019

Ieng-Wai Un , and Yonatan Sivan 

COLLECTIONS

 This paper was selected as Featured



View Online



Export Citation



CrossMark

ARTICLES YOU MAY BE INTERESTED IN

[Generating heat by illuminating gold versus silver nanoparticles](#)

Scilight **2019**, 451102 (2019); <https://doi.org/10.1063/10.0000221>

[Magnetic and Plasmonic Nanoparticles for Biomedical Devices](#)

Journal of Applied Physics **126**, 170401 (2019); <https://doi.org/10.1063/1.5130560>

[On the temperature dependence of the efficiency of electroluminescence](#)

Journal of Applied Physics **126**, 173102 (2019); <https://doi.org/10.1063/1.5124566>

Lock-in Amplifiers

... and more, from DC to 600 MHz



Size-dependence of the photothermal response of a single metal nanosphere



Cite as: J. Appl. Phys. **126**, 173103 (2019); doi: [10.1063/1.5123629](https://doi.org/10.1063/1.5123629)

Submitted: 7 August 2019 · Accepted: 14 October 2019 ·

Published Online: 4 November 2019



View Online



Export Citation



CrossMark

Ieng-Wai Un^{1,2,a)} and Yonatan Sivan¹

AFFILIATIONS

¹School of Electrical and Computer Engineering, Ben-Gurion University of the Negev, Beer-Sheva 8410501, Israel

²Joan and Irwin Jacobs TIX Institute, National Tsing Hua University, Hsinchu 30013, Taiwan

^{a)}Electronic mail: iengwai@post.bgu.ac.il

ABSTRACT

We study the thermal response of a single spherical metal nanoparticle to continuous wave illumination as a function of its size. We show that the particle temperature increases nonmonotonically as the particle size increases, indicating that the photothermal response can be optimized by tuning the particle size and illumination wavelength. We also compare the size-dependence of the photothermal effects of gold and silver nanoparticles and find somewhat surprisingly that Ag nanoparticles are more efficient heat generators only for sufficiently small sizes. These results have importance for applications such as plasmon-assisted photocatalysis, photothermal cancer therapy, etc. and provide a first step toward the study of the size-dependence of the thermo-optic nonlinearity of metal nanospheres.

Published under license by AIP Publishing. <https://doi.org/10.1063/1.5123629>

I. INTRODUCTION

Metal nanoparticles (NPs) have been studied extensively in the last few decades because of their ability to confine and enhance the electromagnetic field to a subwavelength scale. They have found a wide variety of applications^{1,2} such as optical devices in nanoscale,³ optoelectronics,⁴ biological sensing,^{5,6} and biomedicine.^{7,8} In addition to the good field enhancement and scattering properties, plasmonic nanoparticles have been shown to be ideal heating nanosources when subjected to illumination at their plasmonic resonance wavelength.^{9–12} This active research field based on the Joule effect of metal NPs under illumination is usually referred to as thermoplasmonics^{9,11} and has led to a wide range of emerging applications, especially in biology and energy harvesting, e.g., photothermal imaging,^{13–15} photothermal therapy,^{13,16–18} thermophotovoltaics,^{19,20} plasmonic-heating-induced nanofabrication,^{21,22} fluid and molecule dynamics and control in biological applications,^{23–25} water boiling,²⁶ and plasmon-assisted photocatalysis.^{27–32}

Under continuous wave (CW) illumination, the temperature rise of the NP is determined by the balance between the incoming illumination energy flow and an equal flow of heat to the environment. For sufficiently small particles, it is possible to calculate the absorption by employing the so-called quasistatic (QS) approximation. Under this approximation and for fixed illumination intensity,

the particle temperature increases monotonically with the particle size. However, as we shall see, the particle temperature varies nonmonotonically with the particle size in a manner that was not studied thoroughly so far. Therefore, the present study highlights the importance of the size-dependent particle temperature to identifying the optimal conditions for heat generation. In order to avoid additional complexity due to thermo-optic nonlinear effects,^{33–35} i.e., the temperature dependence of the optical and thermal properties of the materials, we limit the illumination intensity in which case the particle temperature rise is lower than 100 K such that the temperature dependence of the thermal and optical parameters can be neglected, as suggested in Ref. 36. We focus on modeling the heat generation from a single metal NP. We trace the nature of the nonmonotonic behavior to the contributions of the electric dipole and quadrupole modes to the absorption cross section of the NP. Finally, we compare the size-dependence of photothermal response of Au and Ag NPs and identify the particle size and illumination wavelength that yield optimal heat generation. We find, somewhat surprisingly, that while Ag NPs are more efficient heat generators for sufficiently small sizes, Au NPs become more efficient for larger NPs.

This work is a first step toward the study of NP arrays^{12,29,37,38} and critical for the optimization of the photothermal effect in all the above mentioned applications. Most importantly, since

thermal effects were shown to be responsible for observations of faster chemical reactions in some of the most famous papers on the topic (see discussion in Refs. 39, 27, 29, and 28), our work can be used to interpret correctly the differences in chemical reaction enhancements originating from the use of metal particles of different sizes.

II. CONFIGURATION AND METHODOLOGY

We consider a “single” spherical metallic NP of radius a in a lossless dielectric host ϵ_h illuminated by a high intensity CW laser. The absorption of incident photons causes the NP to heat up, an effect which is balanced by heat transfer to the environment such that the temperature reaches a steady state. In this case, the heat equation reduces to the Poisson equation,

$$\nabla \cdot (\kappa(\mathbf{r})\nabla T(\mathbf{r})) = -p_{\text{abs}}(\omega, \mathbf{r}), \quad (1)$$

where κ is the thermal conductivity and $p_{\text{abs}}(\omega, \mathbf{r})$ is the absorbed power density. Here, we only consider one-photon absorption and neglect potential multiphoton absorption so that the time averaged absorbed power density is given by $p_{\text{abs}}(\omega, \mathbf{r}) = \frac{\omega}{2} \epsilon_0 \epsilon''(\omega) |\mathbf{E}(\omega, \mathbf{r})|^2$, where $\mathbf{E}(\omega, \mathbf{r})$ is the total (local) electric field. This field and, thus, the absorbed power density can be, in general, obtained by the Mie solution⁴⁰ to the Maxwell’s equations or using a direct numerical simulation. For very small spherical NPs, one can solve Maxwell’s equations based on the quasistatic (QS) approximation.⁴⁰

Since the heat source $p_{\text{abs}}(\omega, \mathbf{r})$ is, in general, spatially-dependent, Eq. (1) has no simple closed-form solution. To obtain an approximate analytic solution of Eq. (1), we replace the spatially nonuniform absorbed power density in Eq. (1) by its volume average (see justification in Appendix A),¹⁰ which can be written as a product of the illumination intensity I_{inc} and the absorption cross section C_{abs} , divided by the volume of the NP, namely, $\bar{p}_{\text{abs}}(\omega) \equiv \frac{3}{4\pi a^3} \frac{\omega \epsilon_0}{2} \int d^3r \epsilon''_m(\omega) |\mathbf{E}(\mathbf{r}, \omega)|^2 = \frac{3}{4\pi a^3} I_{\text{inc}} C_{\text{abs}}(\omega)$. Then, we integrate Eq. (1) and apply the Gauss law to convert the volume integral on the left hand side into a surface integral and then integrate over the radius. We obtain¹⁰

$$\begin{cases} T(r) = T_h + \frac{\bar{p}_{\text{abs}}(\omega)a^2}{3\kappa_h} \left[1 + \frac{\kappa_h}{2\kappa_m} \left(1 - \frac{r^2}{a^2} \right) \right], & \text{for } r \leq a, \\ T(r) = T_h + \frac{\bar{p}_{\text{abs}}(\omega)a^3}{3\kappa_h r}, & \text{for } r \geq a, \end{cases} \quad (2)$$

where $T_{h,0}$ is the ambient temperature. Equation (2) shows that the variation of the temperature inside the NP is at the order of $\sim \kappa_h/\kappa_m$, which is small for common gas and liquid hosts but can be substantial for dielectric solid hosts, e.g., for semiconductors.⁴¹ The approximate analytic solution (2) is shown to be in excellent agreement with the simulated temperature distribution in Appendix A [see Fig. 7(b)].⁴² Thus, it justifies (*a posteriori*) the neglect of the spatial dependence of absorbed power density, and more generally, of the results of previous studies of the nonlinear thermo-optic response that relied on the uniform temperature assumption.^{35,36}

Hereafter, we denote the particle temperature T_{NP} by its surface temperature,

$$T_{\text{NP}} = T_h + \frac{\bar{p}_{\text{abs}}(\omega)a^2}{3\kappa_h} = T_h + \frac{C_{\text{abs}}(\omega)I_{\text{inc}}(\omega)}{4\pi\kappa_h a}. \quad (3)$$

We also label the solution (3) with C_{abs} obtained from the Mie theory and from the QS approximation as the Mie-heat solution and the QS-heat solution, respectively. Having established the similarity of the exact numerical solution with the Mie solution, we focus in what follows on the Mie solution and the differences from the QS solution.

III. TEMPERATURE OF NANOPARTICLES OF DIFFERENT SIZES

A. A heuristic analysis

The solution of Eq. (3) implies that, in general, $\Delta T_{\text{NP}} \equiv T_{\text{NP}} - T_{h,0} \sim C_{\text{abs}}/(\kappa_h a)$. For NPs sufficiently small with respect to the wavelength, the electric field within the NP is uniform such that the absorption cross section is given by the QS approximation⁴⁰

$$C_{\text{abs,qs}} = \frac{12\pi\epsilon_h\epsilon''_m}{(\epsilon'_m + 2\epsilon_h)^2 + \epsilon''_m{}^2} ka^3, \quad (4)$$

which scales as a^3/λ . In this case, the increase of the particle temperature is given by

$$\Delta T_{\text{NP,qs}} = \frac{ka^2 I_{\text{inc}}}{\kappa_h} \frac{3\epsilon_h\epsilon''_m}{(\epsilon'_m + 2\epsilon_h)^2 + \epsilon''_m{}^2}, \quad (5)$$

which scales quadratically with the radius. In contrast, for NPs sufficiently large with respect to the skin depth ($a > 200$ nm for visible wavelengths), the total absorbed power originates mainly from the surface layer of the particle and is approximately proportional to a^2 . In this case, one expects the particle temperature to be proportional to a , i.e., to show a slower (yet monotonic) increase of temperature. However, for NP sizes lying between these two extremes, the numerical results below show that the particle temperature undergoes much more complex variations with the particle size, due to the nontrivial modal response of the particle. We show this through numerical examples.

B. Numeric results—Au NPs

In Fig. 1, we show the QS-heat [Eq. (5)] and the Mie-heat solutions of Eq. (1) for gold NPs of different sizes immersed in oil at wavelengths of 532 nm, 560 nm, and 594 nm for a fixed incoming intensity of 40 kW/cm². We also show the contribution from the electric dipole and electric quadrupole modes to the Mie-heat solutions. The permittivity of Au is taken from Ref. 43, and the dielectric permittivity and thermal conductivity of the host are set to be $\epsilon_h = 2.25$ and $\kappa_h = 0.35$, respectively. For sufficiently small particle sizes ($a \lesssim 10$ nm), the Mie-heat solutions show that ΔT_{NP}

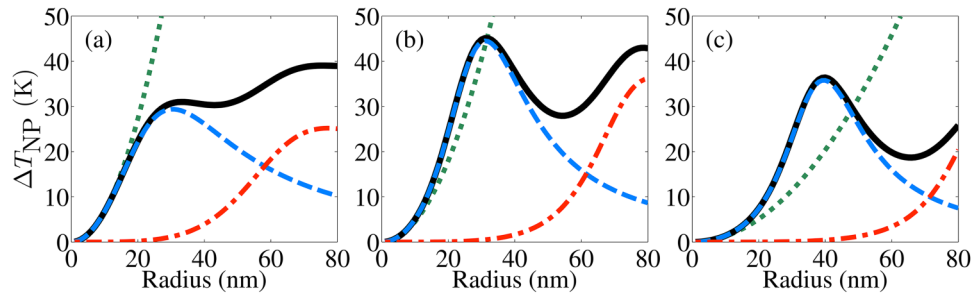


FIG. 1. The temperature rise of gold NP in oil given by the QS-heat method [Eq. (5), green dots] and the Mie-heat method (black solid line) as a function of particle radius a under illumination with fixed incoming intensity 40 kW/cm^2 at wavelength (a) 532 nm, (b) 560 nm, and (c) 594 nm. For the Mie-heat method, the contribution from the electric dipole and electric quadrupole to the particle temperature rise is represented by the blue dashed line and the red dashed-dotted line, respectively.

increases quadratically with the radius, in agreement with the QS-heat solution Eq. (5); this verifies the validity of the results in Refs. 35 and 36 for such small NPs.

However, for larger NPs, the behavior is more complicated. Specifically, ΔT_{NP} increases with the particle radius at a lower and somewhat oscillatory rate for $\lambda = 532 \text{ nm}$ [see Fig. 1(a)]. For the longer wavelengths, ΔT_{NP} exhibits a more interesting behavior [see Figs. 1(b) and 1(c)]. Specifically, for $\lambda = 560 \text{ nm}$, the particle temperature rise given by the Mie-heat solution is $\sim 10\%$ “higher” than that given by the QS-heat solution for particle radius of $15 \text{ nm} \lesssim a \lesssim 35 \text{ nm}$. For even larger particles, the size-dependence of ΔT_{NP} exhibits an oscillatory behavior, which is not captured by the heuristic analysis above. For $\lambda = 594 \text{ nm}$, the oscillatory size-dependence of ΔT_{NP} is similar to the case of $\lambda = 560 \text{ nm}$, but the range of sizes for which the Mie-heat temperature is higher than the QS-heat solution is wider and the temperature difference is greater ($\sim 30\%$).

Both the higher particle temperature predicted by the Mie-heat solution and the nonmonotonic size-dependence of the particle temperature can be attributed to the contribution of various multipoles to the absorption cross section and the size-induced red-shift in their resonance frequencies. In order to see that, we show in Fig. 2 and analyze in Appendix B the contributions to the absorption cross section from the electric dipole and electric quadrupole modes for Au NPs of different sizes. One can see from Fig. 2 that for particle sizes of $a < 50 \text{ nm}$, the electric dipole mode dominates the absorption cross section and that its contribution increases and shifts from 550 nm to longer wavelengths and then decreases in its quality factor as the particle size increases [see also Eqs. (B6) and (B8)]. The red-shift of the electric dipole resonance from 550 nm makes the illumination at longer wavelengths closer to resonance, an effect which is not captured by the QS approximation. This not only explains the faster growing rate of the Mie-heat temperature compared to that of the QS-heat solution for small particle sizes, but also explains that such faster growing rate only occurs for wavelength longer than 550 nm. Secondly, for particle sizes of $a = 50 \text{ nm}$, the electric quadrupole mode shows up at around 550 nm. As the particle size further increases, the electric dipole resonance shifts to a wavelength longer than 600 nm, but its resonance strength becomes very weak due to the decrease of the quality factor (see Appendix B). Meanwhile, the

electric quadrupole mode contribution gets stronger, shifts to longer wavelengths, and then dominates over the electric dipole mode. The further shift and weakening of the electric dipole response, as well as the emergence of the electric quadrupole mode explains the nonmonotonic dependence of particle temperature on the particle size for wavelengths longer than 550 nm.

C. Numeric results—Ag NPs

We now replace the Au NP with a Ag NP, and all other parameters remain the same as in Sec. III B. Figures 3(a) and 3(b) show the comparison of the size-dependent particle temperature

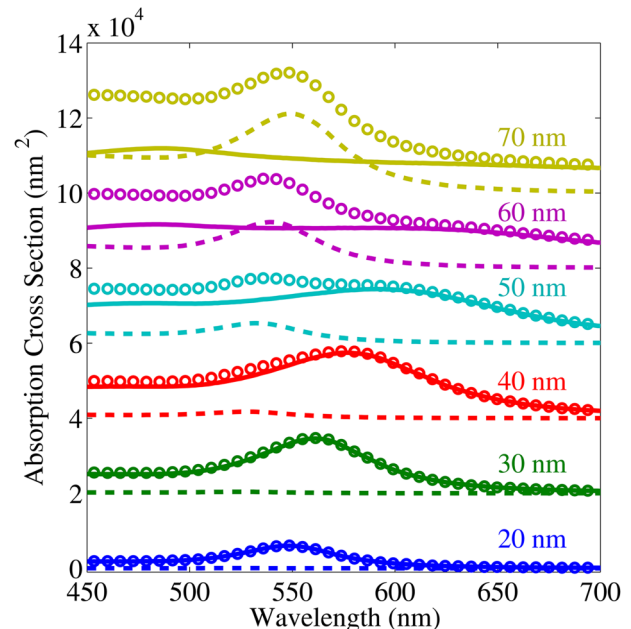


FIG. 2. The (linear) absorption cross section of gold NPs of different sizes immersed in oil. The contribution from the electric dipole (solid line) and electric quadrupole mode (dashed line) to the total absorption cross section (circles) is shown separately.

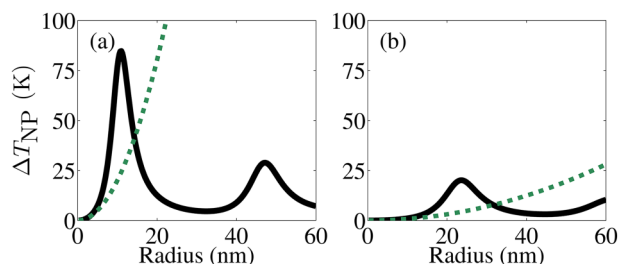


FIG. 3. The temperature rise of a Ag NP in oil given by the QS-heat method (green dots) and the Mie-heat method (black solid line) as a function of particle radius a under illumination of 40 kW/cm^2 at wavelength (a) 420 nm and (b) 450 nm .

between the QS-heat solution equation (5) and the Mie-heat solution for Ag NP under illumination intensity 20 kW/cm^2 at wavelength 420 nm (the plasmon resonance wavelength for small Ag spheres in oil) and 450 nm , respectively. The particle size range in which the QS-heat solution equation (5) agrees with the more accurate Mie-heat solution is now much smaller than 10 nm . The nonmonotonic size-dependence of the Ag NP temperature is again due to the red-shift of the electric dipole resonance and due to the emergence of the quadrupole resonance, qualitatively similar to the case of Au NPs. In similarity to Fig. 2, we show in Fig. 4 the contributions to the absorption cross section from the

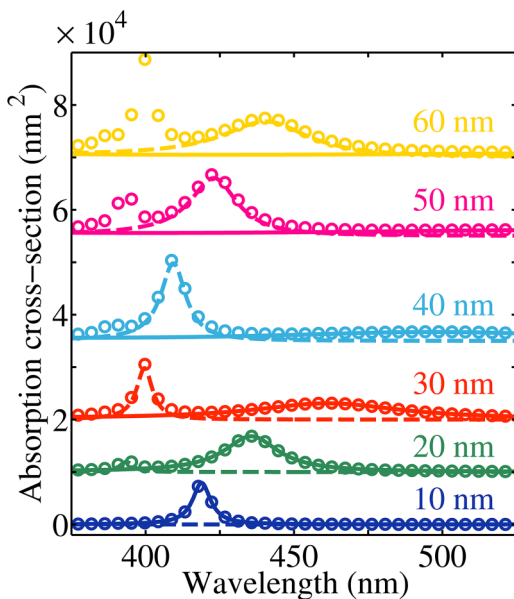


FIG. 4. The (linear) absorption cross section of silver NPs of different sizes immersed in oil. The contribution from the electric dipole (solid line) and electric quadrupole mode (dashed line) to the total absorption cross section (circles) are shown separately.

dipole and quadrupole modes for Ag NPs of different sizes. One can see that the electric dipole mode dominates for particle size $a < 20 \text{ nm}$ and its resonance wavelength shifts from 420 nm to 470 nm when the NP radius increases from 10 nm to 30 nm . For $a = 30 \text{ nm}$, the electric quadrupole mode emerges at $\lambda \approx 400 \text{ nm}$. This resonance shifts from 400 nm to 445 nm when the NP radius increases from 30 nm to 60 nm . These observations explain the local maxima of the NP temperature rise at $a \approx 10 \text{ nm}$ and $a \approx 50 \text{ nm}$ for $\lambda = 420 \text{ nm}$. In addition, since the quality factor decreases as the particle size increases [see Eqs. (B6) and (B8)], the size-induced red-shifted resonance at $\lambda = 450 \text{ nm}$ becomes much weaker than that at $\lambda = 420 \text{ nm}$, such that the NP temperature rise at $\lambda = 450 \text{ nm}$ is much lower than that at $\lambda = 420 \text{ nm}$. The difference in the nonmonotonic size-dependence between Ag and Au NPs is caused by the much smaller value of $|\epsilon_m''/\epsilon_m'|$ for Ag than that of Au.

IV. DISCUSSION

The oscillatory size-dependence of the particle temperature rise shown in the numerical examples above implies that there exists an optimal size of NPs as nanoheating sources for each wavelength. Specifically, since the plasmonic resonance shifts to longer wavelengths when the particle size increases, one can further optimize the performance of the photothermal response by choosing the illumination wavelength to match the plasmonic resonance of the metal NP. For example, we show in Fig. 5(a) the size-dependence of the dipole and quadrupole resonance wavelengths for Au and Ag NPs, and show in Figs. 5(b) and 5(c) the size-dependence of the particle temperature rise at the corresponding resonance wavelength. The combination of Fig. 5 shows that under the electric dipole (quadrupole) resonance condition, the highest temperature rise occurs at $a = 32 \text{ nm}$ and $\lambda = 564 \text{ nm}$ ($a = 86 \text{ nm}$ and $\lambda = 572 \text{ nm}$) for Au and $a = 10 \text{ nm}$ and $\lambda = 420 \text{ nm}$ ($a = 40 \text{ nm}$ and $\lambda = 410 \text{ nm}$) for Ag NPs. In addition, for the electric dipole (quadrupole) resonance, the temperature rise of Ag NP is higher than that of Au NP only for particle size $a < 20 \text{ nm}$ ($a < 60 \text{ nm}$). These optimal values of size are critical for choosing Au or Ag for application such as heat generation.

The size-dependence of the particle temperature rise under the electric dipole resonance condition (B6) can be understood by the Padé approximation for the absorption cross section (B8). As the particle size increases, the absorption cross section (B8) first increases with the NP volume (x^3 in the numerator) and then it is subsequently enhanced due to the dynamic depolarization effect (x^2 in the numerator and the denominator) and finally is suppressed due to radiation damping (x^3 in the denominator). Equation (B8) can also be used to explain the material-dependence of the particle temperature rise. For small particle sizes, the absorption cross section (B8) is “inversely” proportional to ϵ_m'' , so the temperature rise is higher for low loss metal NP, in agreement with previous results.^{11,36,64} However, when the particle size increases and becomes large enough so that the radiation damping term [x^3 term in the denominator of (B8)] dominates, the absorption cross section becomes “directly” proportional to ϵ_m'' , so the temperature rise is higher for lossy metal NPs. The size- and material-dependence of the temperature rise associated with the electric

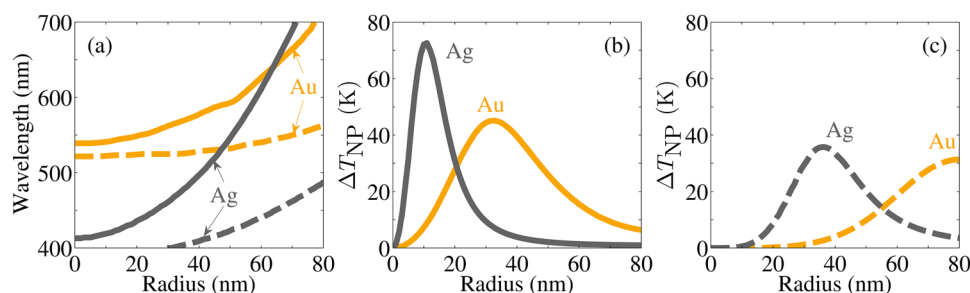


FIG. 5. (a) The resonance wavelength and the particle temperature rise of Au and Ag NPs in oil as a function of particle radius a under illumination of 40 kW/cm^2 at (b) the electric dipole and (c) the electric quadrupole resonance conditions. The solid and dashed lines represent the electric dipole and quadrupole modes, respectively.

quadrupole resonance are qualitatively similar to those of the electric dipole resonance except that $\Delta T_{\text{NP}} \sim a^4$ for small particle sizes [see Eq. (B9)].

The oscillatory size-dependence of particle temperature rise shown in Figs. 1 and 3 can be used to explain the results of various previous experiments. Specifically, we show in Fig. 6 the size-dependence of the illumination intensity (at wavelength 560 nm) required to increase a Au NP temperature by 40 K. This provides a simple theoretical explanation to the empirical observation of a local minimum of the size-dependent fluence threshold for photothermal bubble generation in various previous papers.^{44–46}

In addition to the physical insights it provides, our study is also an important step toward achieving a quantitative match between experimental results and verifying the thermal effect^{35,36} being the underlying mechanism responsible for the nonlinear scattering of CW illumination observed in Refs., 47, 33, and 34. The results of this study cannot only be applicable to a single NP system,^{33,34,47} but also are the basis for studies of NP arrays. Specifically, the temperature increase of a many-particle array can be obtained by summing properly the heat generated by all particles in the system.^{12,29} Based on this approach, it has been shown that the heat generation from NP array is much more significant than that from single NP.^{12,29,37,38} Recently, it has also been revealed that the photothermal effect of the NP array plays an important role in the

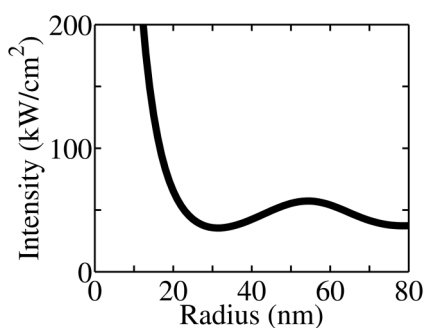


FIG. 6. The size-dependence of the incoming intensity required to increase the Au NP temperature by 40 K. The Au NP is immersed in oil and the wavelength of the illumination is 560 nm.

electrochemical current enhancement in the plasmonic system.³⁸ Therefore, the optimal NP size and wavelength for single NP can be used to maximize the heat generation from NP arrays.

We should mention that our model can be further improved. For example, Meng *et al.*⁴⁸ used the more accurate two-temperature model⁴⁹ that accounts for the differences between the electron and lattice temperatures and accounts for the Kapitza Refs. 50–55. This study also showed that the photothermal response can be further improved by carefully adding multiple metal shells.

Finally, we note that if one is interested in studying the thermal response for a temperature rise greater than 100 K, it is necessary to take into account the temperature dependence of the optical and thermal properties of the metal (and its surroundings) when calculating the field and temperature under intense illumination conditions.³⁵ A complete temperature-dependent and size-dependent model for the photothermal response will have to be left for a future study.

ACKNOWLEDGMENTS

Y.S. and I.-W.U. were partially supported by the Israel Science Foundation (ISF) under Grant No. 899/16. I.-W.U. was partially supported by the Joan and Irwin Jacobs TIX Institute at National Tsing Hua University in Taiwan.

APPENDIX A: NON-UNIFORMITY OF THE ABSORBED POWER DENSITY AND THE TEMPERATURE WITHIN THE NANOPARTICLE

In this Appendix, we study the uniformity of the absorbed power density and the temperature within the NP, and verify the usage of the uniform \bar{p}_{abs} to obtain the approximate analytic solution equation (2). We used COMSOL Multiphysics to solve Maxwell's equations to obtain the electromagnetic fields and $p_{\text{abs}}(\omega, \mathbf{r})$ and then solved Eq. (1) to obtain the temperature distribution. For solving Maxwell's equations, a plane-wave illumination was set by using a port boundary condition; perfectly matched layers and scattering boundary conditions were used in the surrounding boundaries in order to eliminate unphysical reflections. For the temperature calculations, we applied transformation optics to the heat equation^{56,57} and carefully assigned the perfectly matched layers with an anisotropic thermal conductivity to reduce

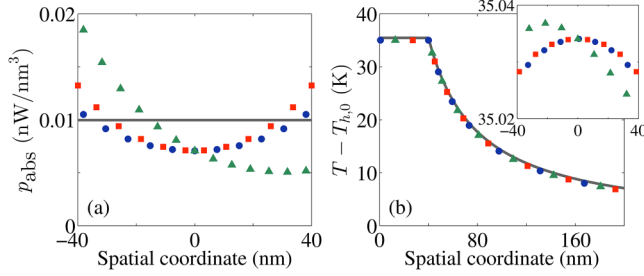


FIG. 7. (a) The absorbed power density and (b) the temperature distribution of a single Au NP (40 nm in radius) in oil under an illumination (y-polarized, incidence along the z-axis) with intensity 40 kW/cm² at a wavelength of 532 nm. The black solid line represents the averaged absorbed power density \bar{p}_{abs} in (a) and the approximate analytic Mie-heat solution (2) in (b). The blue-circle, red-square, and green-triangle dots represent the COMSOL simulation results along the x-, y- and z-axis, respectively. The inset in (b) shows the zoomed-in region of the NP.

the volume of the simulation domain. This approach is potentially more accessible compared with the volume integral simulation techniques described in Ref. 58.

Figure 7 shows the COMSOL simulation results of the absorbed power density and the temperature distribution of a single Au NP of 40 nm in radius subjected to CW illumination at wavelength 532 nm. The numeric solution shows that the temperature and absorbed power density inside the NP are spatially non-uniform due to the decay of the local field away from the metal-dielectric interface. In addition, the absorbed power density along the z axis is different from that along the x and y axes. This happens due to the constructive interference of the electric dipole and quadrupole moments along the axial direction.⁴⁰ However, while the absorbed power density nonuniformity might be significant (~25%–50%, especially, when high-order multipoles are excited), the NP temperature nonuniformity is quite small [$< 0.06\%$, see the inset in Fig. 7(b)]. This is in agreement with simulations performed previously even for strongly asymmetric particles and/or sources,¹⁰ which also showed that the reason for the weak nonuniformity is the high thermal conductivity of the metal.

APPENDIX B: DETAILED ANALYSIS OF THE SIZE-DEPENDENCE OF THE ABSORPTION CROSS SECTION

In this Appendix, we analyze in detail the size-dependence of the absorption cross section of a nanosphere. Based on Mie theory,⁴⁰ the absorption cross section can be quantified by the Mie coefficients, denoted by a_n 's and b_n 's. Since we are interested only in metallic NPs, in this analysis we will focus on a_n 's, which are responsible for the plasmonic resonance. The electric Mie coefficient a_n is given by⁴⁰

$$a_n = \frac{m\psi_n(mx)\psi_n'(x) - \psi_n(x)\psi_n'(mx)}{m\psi_n(mx)\xi_n'(x) - \xi_n(x)\psi_n'(mx)}, \quad (B1)$$

where $m = \sqrt{\epsilon_m/\epsilon_h}$ is the contrast parameter, $x = ka$ is the size parameter, $k = \sqrt{\epsilon_h\omega}/c_0$ is the wavenumber of the host, while $\psi_n(\rho)$ and $\xi_n(\rho)$ are the Riccati-Bessel functions,

$$\psi_n(\rho) = \rho j_n(\rho), \quad \xi_n(\rho) = \rho h_n^{(1)}(\rho). \quad (B2)$$

By applying the Padé approximants,^{59,60} the first electric Mie coefficient a_1 is approximated by

$$a_1^{[3/3]} \approx \frac{-i^2 \frac{\epsilon_m - \epsilon_h}{3\epsilon_m + 2\epsilon_h} x^3}{1 - \frac{3\epsilon_m - 2\epsilon_h}{5\epsilon_m + 2\epsilon_h} x^2 - i^2 \frac{\epsilon_m - \epsilon_h}{3\epsilon_m + 2\epsilon_h} x^3} \equiv -\frac{2i}{3} \frac{(\epsilon_m - \epsilon_h)x^3}{q_1(\epsilon_m', \epsilon_m'', \epsilon_h, x) + iq_2(\epsilon_m', \epsilon_m'', \epsilon_h, x)}, \quad (B3)$$

where r and s in $[r/s]$ denote the highest order of the polynomial in the numerator and denominator of the Padé approximated function, respectively. Specifically,

$$q_1(\epsilon_m', \epsilon_m'', \epsilon_h, x) = \epsilon_m' \left(1 - \frac{3}{5}x^2\right) + 2\epsilon_h \left(1 + \frac{3}{5}x^2\right) + \frac{2}{3}\epsilon_m''x^3 \quad (B4)$$

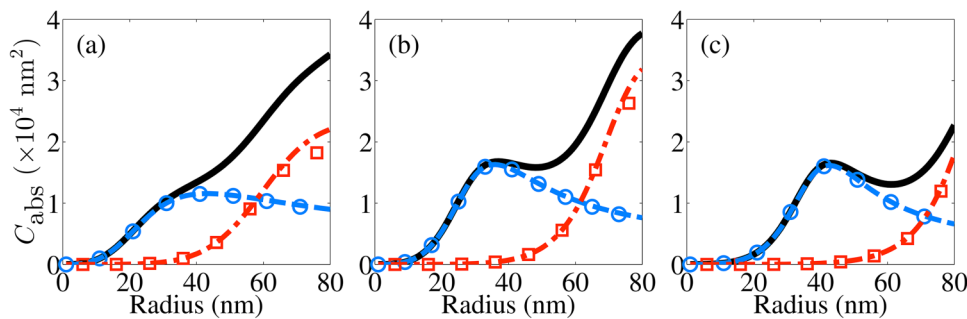


FIG. 8. The absorption cross section of gold NP in oil given by the Mie theory (black solid line) as a function of particle radius a at wavelength (a) 532 nm, (b) 560 nm, and (c) 594 nm. The contribution from the electric dipole and electric quadrupole to the absorption cross section (and their Padé approximation) are represented by blue dashed line (blue circles) and red dashed-dotted line (red squares), respectively.

and

$$q_2(\epsilon'_m, \epsilon''_m, \epsilon_h, x) = \epsilon''_m \left(1 - \frac{3}{5}x^2 \right) - \frac{2}{3}(\epsilon'_m - \epsilon_h)x^3. \quad (\text{B5})$$

The x^2 and x^3 terms in the denominator are, respectively, recognized as the dynamic depolarization⁶¹ and radiation damping.⁶² The dipole resonance condition can be determined by the zero of the real part of the denominator of $a_1^{[3/3]}$, i.e., $q_1 = 0$, which is satisfied for

$$\epsilon'_m = \frac{-2\epsilon_h(1 + 3x^2/5) - 2\epsilon''_m x^3/3}{1 - 3x^2/5}. \quad (\text{B6})$$

The quality factor of the resonance is determined by the imaginary part of the denominator of $a_1^{[3/3]}$, i.e., q_2 . One can clearly see the red-shift and the reduction in the quality factor of the dipole resonance from Eqs. (B6) and (B5) due to the increase of particle size.

The contribution of the electric dipole to the absorption cross section can be explicitly written as

$$C_{\text{abs}}^{\text{ed}[3/3]} = \frac{6\pi}{k^2} \left[\text{Re}(a_1^{[3/3]}) - |a_1^{[3/3]}|^2 \right] \approx \frac{12\pi \epsilon''_m \epsilon_h x^3 (1 + x^2)}{k^2 (q_1^2 + q_2^2)}. \quad (\text{B7})$$

The electric dipole absorption cross section under resonance condition can be obtained by substituting Eq. (B6) into Eq. (B7)

$$C_{\text{abs.res}}^{\text{ed}[3/3]} \approx \frac{12\pi}{k^2} \frac{\epsilon''_m \epsilon_h x^3 (1 + x^2)}{[\epsilon''_m (1 - 3x^2/5) - 2(\epsilon'_m - \epsilon_h)x^3/3]^2}. \quad (\text{B8})$$

The Padé approximated second electric Mie coefficient a_2 can be obtained similarly⁶³

$$a_2^{[5/5]} \approx \frac{-\frac{i}{15} \frac{\epsilon_m - \epsilon_h}{2\epsilon_m + 3\epsilon_h} x^5}{1 + \frac{5}{7} \frac{\epsilon_h}{2\epsilon_m + 3\epsilon_h} x^2 - \frac{5}{1323} \frac{\epsilon_m^2 + 30\epsilon_m \epsilon_h - 45\epsilon_h^2}{\epsilon_h(2\epsilon_m + 3\epsilon_h)} x^4 - \frac{i}{15} \frac{\epsilon_h}{2\epsilon_m + 3\epsilon_h} x^5}. \quad (\text{B9})$$

After some lengthy algebra, one can see from $C_{\text{abs}}^{\text{eq}[5/5]} = \frac{10\pi}{k^2} \left[\text{Re}(a_2^{[5/5]}) - |a_2^{[5/5]}|^2 \right]$ that $C_{\text{abs}}^{\text{eq}[5/5]}$ changes with the particle size in a similar way to $C_{\text{abs}}^{\text{ed}[3/3]}$ except that $C_{\text{abs}}^{\text{eq}[5/5]} \sim x^5$ for small particle size.

In Fig. 8, we show a comparison of size-dependent C_{abs} of a single Au NP between the Mie theory and the Padé approximation. The Padé approximation shows excellent agreement with the Mie theory for particle size $a \leq 60$ nm.

REFERENCES

¹J. A. Schuller, E. S. Barnard, W. Cai, Y. C. Jun, J. S. White, and M. L. Brongersma, "Plasmonics for extreme light concentration and manipulation," *Nat. Mater.* **9**, 193–204 (2010).

²V. Giannini, A. I. Fernández-Domínguez, S. C. Heck, and S. A. Maier, "Plasmonic nanoantennas: Fundamentals and their use in controlling the radiative properties of nanoemitters," *Chem. Rev.* **111**, 3888–3912 (2011).

³S. A. Maier, M. L. Brongersma, P. G. Kik, S. Meltzer, A. A. G. Requicha, and H. A. Atwater, "Plasmonics—A route to nanoscale optical devices," *Adv. Mater.* **13**, 1501–1505 (2001).

⁴P. V. Kamat, "Photophysical, photochemical and photocatalytic aspects of metal nanoparticles," *J. Phys. Chem. B* **106**, 7729–7744 (2002).

⁵P. K. Jain, X. Huang, I. H. El-Sayed, and M. A. El-Sayed, "Noble metals on the nanoscale: Optical and photothermal properties and some applications in imaging, sensing, biology, and medicine," *Acc. Chem. Res.* **41**, 1578–1586 (2008).

⁶K. Saha, S. S. Agasti, C. Kim, X. Li, and V. M. Rotello, "Gold nanoparticles in chemical and biological sensing," *Chem. Rev.* **112**, 2739–2779 (2012).

⁷L. A. Dykman and N. G. Khlebtsov, "Gold nanoparticles in biology and medicine: Recent advances and prospects," *Acta Nat.* **3**, 34–55 (2011).

⁸E. C. Dreaden, A. M. Alkilany, X. Huang, C. J. Murphy, and M. A. El-Sayed, "The golden age: Gold nanoparticles for biomedicine," *Chem. Soc. Rev.* **41**, 2740–2779 (2012).

⁹A. O. Govorov and H. H. Richardson, "Generating heat with metal nanoparticles," *Nano Today* **2**, 30–38 (2007).

¹⁰G. Baffou, R. Quidant, and F. J. García de Abajo, "Nanoscale control of optical heating in complex plasmonic systems," *ACS Nano* **4**, 709–716 (2010).

¹¹G. Baffou and R. Quidant, "Thermo-plasmonics: Using metallic nanostructures as nano-sources of heat," *Laser Photon. Rev.* **7**, 171–187 (2013).

¹²G. Baffou, P. Berto, E. Bermúdez Ureña, R. Quidant, S. Monneret, J. Polleux, and H. Rigneault, "Photoinduced heating of nanoparticle arrays," *ACS Nano* **7**, 6478–6488 (2013).

¹³O. Blum and N. T. Shaked, "Prediction of photothermal phase signatures from arbitrary plasmonic nanoparticles and experimental verification," *Light Sci. Appl.* **4**, e322 (2015).

¹⁴D. Boyer, P. Tamarat, A. Maali, B. Lounis, and M. Orrit, "Photothermal imaging of nanometer-sized metal particles among scatterers," *Science* **297**, 1160–1163 (2002).

¹⁵L. Cognet, S. Berciaud, D. Lasne, and B. Lounis, "Photothermal methods for single nonluminescent nano-objects," *Anal. Chem.* **80**, 2288–2294 (2008).

¹⁶M. B. Cortie, D. L. Cortie, and V. Timchenko, "Heat transfer from nanoparticles for targeted destruction of infectious organisms," *Int. J. Hyperthermia* **34**, 157–167 (2018).

¹⁷R. S. Riley and E. S. Day, "Gold nanoparticle-mediated photothermal therapy: Applications and opportunities for multimodal cancer treatment," *Wiley Interdiscipl. Rev. Nanomed. Nanobiotechnol.* **9**, e1449 (2017).

¹⁸J. B. Vines, J. H. Yoon, N. E. Ryu, D. J. Lim, and H. Park, "Gold nanoparticles for photothermal cancer therapy," *Front. Chem.* **7**, 167 (2019).

¹⁹S. Molesky, C. J. Dewalt, and Z. Jacob, "High temperature epsilon-near-zero and epsilon-near-pole metamaterial emitters for thermophotovoltaics," *Opt. Express* **21**, A96–A110 (2013).

²⁰J. Liu, U. Guler, A. Lagutchev, A. Kildishev, O. Malis, A. Boltasseva, and V. M. Shalaev, "Quasi-coherent thermal emitter based on refractory plasmonic materials," *Opt. Mater. Express* **5**, 2721–2728 (2015).

²¹Y. Osaka, S. Sugano, and S. Hashimoto, "Plasmonic-heating-induced nanofabrication on glass substrates," *Nanoscale* **8**, 18187–18196 (2016).

²²M. Enders, S. Mukai, T. Uwada, and S. Hashimoto, "Plasmonic nanofabrication through optical heating," *J. Phys. Chem. C* **120**, 6723–6732 (2016).

²³D. Andrén, L. Shao, N. Odebo Länk, S. S. Acimović, P. Johansson, and M. Käll, "Probing photothermal effects on optically trapped gold nanorods by simultaneous plasmon spectroscopy and Brownian dynamics analysis," *ACS Nano* **11**, 10053–10061 (2017).

²⁴H. Šípová, L. Shao, N. Odebo Länk, D. Andrén, and M. Käll, "Photothermal DNA release from laser-tweezed individual gold nanomotors driven by photon angular momentum," *ACS Photonics* **5**, 2168–2175 (2018).

²⁵S. Jones, D. Andrén, P. Karpinski, and M. Käll, "Photothermal heating of plasmonic nanoantennas: Influence on trapped particle dynamics and colloid distribution," *ACS Photonics* **5**, 2878–2887 (2018).

- ²⁶O. Neumann, A. S. Urban, J. Day, S. Lal, P. Nordlander, and N. J. Halas, "Solar vapor generation enabled by nanoparticles," *ACS Nano* **7**, 42–49 (2013).
- ²⁷Y. Sivan, I. W. Un, and Y. Dubi, "Assistance of metal nanoparticles in photocatalysis—Nothing more than a classical heat source," *Faraday Discuss.* **214**, 215–233 (2019).
- ²⁸Y. Sivan, J. Baraban, I. W. Un, and Y. Dubi, "Comment on "Quantifying hot carrier and thermal contributions in plasmonic photocatalysis"," *Science* **364**, eaaw9367 (2019).
- ²⁹Y. Sivan, I. W. Un, and Y. Dubi, "Thermal effects—An alternative mechanism for plasmonic-assisted photo-catalysis," e-print [arXiv:1902.03169](https://arxiv.org/abs/1902.03169) (2019).
- ³⁰J. Aizpurua *et al.*, "Theory of hot electrons: General discussion," *Faraday Discuss.* **214**, 245–281 (2019).
- ³¹J. Aizpurua *et al.*, "Dynamics of hot electron generation in metallic nanostructures: General discussion," *Faraday Discuss.* **214**, 123–146 (2019).
- ³²X. Li, X. Zhang, H. O. Everitt, and J. Liu, "Light-induced thermal gradients in ruthenium catalysts significantly enhance ammonia production," *Nano Lett.* **19**, 1706–1711 (2019).
- ³³S. W. Chu, H. Y. Wu, Y. T. Huang, T. Y. Su, H. Lee, Y. Yonemaru, M. Yamanaka, R. Oketani, S. Kawata, S. Shoji, and K. Fujita, "Saturation and reverse saturation of scattering in a single plasmonic nanoparticle," *ACS Photonics* **1**, 32–37 (2014).
- ³⁴Y. T. Chen, P. H. Lee, P. T. Shen, J. Launer, R. Oketani, K. Y. Li, Y. T. Huang, K. Masui, S. Shoji, K. Fujita, and S. W. Chu, "Study of nonlinear plasmonic scattering in metallic nanoparticles," *ACS Photonics* **3**, 1432–1439 (2016).
- ³⁵Y. Sivan and S. W. Chu, "Nonlinear plasmonics at high temperatures," *Nanophotonics* **6**, 317 (2017).
- ³⁶I. Gurwich and Y. Sivan, "Metal nanospheres under intense continuous-wave illumination: A unique case of nonperturbative nonlinear nanophotonics," *Phys. Rev. E* **96**, 012212 (2017).
- ³⁷D. A. Boyd, L. Greengard, M. Brongersma, M. Y. El-Naggar, and D. G. Goodwin, "Plasmon-assisted chemical vapor deposition," *Nano Lett.* **6**, 2592–2597 (2006).
- ³⁸M. Maley, J. W. Hill, P. Saha, J. D. Walmsley, and C. M. Hill, "The role of heating in the electrochemical response of plasmonic nanostructures under illumination," *J. Phys. Chem. C* **123**, 12390–12399 (2019).
- ³⁹Y. Dubi and Y. Sivan, "Hot electrons" in metallic nanostructures—Non-thermal carriers or heating?" *Light Sci. Appl. Nat.* **8**(1), 89 (2019).
- ⁴⁰C. F. Bohren and D. R. Huffman, *Absorption and Scattering of Light by Small Particles* (John Wiley & Sons, 2008).
- ⁴¹D. R. Lide, *CRC Handbook of Chemistry and Physics: A Ready-Reference Book of Chemical and Physical Data* (CRC Press, 1995).
- ⁴²The simulation domain was equivalent to a cubic box of edge length of $4\ \mu\text{m}$. Since we set the temperature to 300 K on the outer boundary, the simulated temperature distribution is around 0.4 K (1%) lower than the approximate analytic solution equation (2).
- ⁴³P.-T. Shen, Y. Sivan, C.-W. Lin, H.-L. Liu, C.-W. Chang, and S.-W. Chu, "Temperature- and roughness-dependent permittivity of annealed/unannealed gold films," *Opt. Express* **24**, 19254–19263 (2016).
- ⁴⁴E. Lukianova-Hleb, Y. Hu, L. Latterini, L. Tarpani, S. Lee, R. A. Drezek, J. H. Hafner, and D. O. Lapotko, "Plasmonic nanobubbles as transient vapor nanobubbles generated around plasmonic nanoparticles," *ACS Nano* **4**, 2109–2123 (2010).
- ⁴⁵T. Katayama, K. Setoura, D. Werner, H. Miyasaka, and S. Hashimoto, "Picosecond-to-nanosecond dynamics of plasmonic nanobubbles from pump-probe spectral measurements of aqueous colloidal gold nanoparticles," *Langmuir* **30**, 9504–9513 (2014).
- ⁴⁶K. Metwally, S. Mensah, and G. Baffou, "Fluence threshold for photothermal bubble generation using plasmonic nanoparticles," *J. Phys. Chem. C* **119**, 28586–28596 (2015).
- ⁴⁷S. W. Chu, T. Y. Su, R. Oketani, Y. T. Huang, H. Y. Wu, Y. Yonemaru, M. Yamanaka, H. Lee, G. Y. Zhuo, M. Y. Lee, S. Kawata, and K. Fujita, "Measurement of a saturated emission of optical radiation from gold nanoparticles: Application to an ultrahigh resolution microscope," *Phys. Rev. Lett.* **112**, 017402 (2014).
- ⁴⁸L. Meng, R. Yu, M. Qiu, and F. J. Garcia de Abajo, "Plasmonic nano-oven by concatenation of multishell photothermal enhancement," *ACS Nano* **11**, 7915–7924 (2017).
- ⁴⁹S. Anisimov, B. Kapeliovich, and T. Perel'man, "Electron emission from metal surfaces exposed to ultrashort laser pulses," *Sov. Phys. JETP* **39**, 375–377 (1974); available at <http://www.jetp.ac.ru/cgi-bin/e/index/e/39/2/p375?a=list>
- ⁵⁰G. L. Pollack, "Kapitza resistance," *Rev. Mod. Phys.* **41**, 48–81 (1969).
- ⁵¹E. T. Swartz and R. O. Pohl, "Thermal boundary resistance," *Rev. Mod. Phys.* **61**, 605–668 (1989).
- ⁵²X. Chen, A. Munjiza, K. Zhang, and D. Wen, "Molecular dynamics simulation of heat transfer from a gold nanoparticle to a water pool," *J. Phys. Chem. C* **118**, 1285–1293 (2014).
- ⁵³C. Monachon, L. Weber, and C. Dames, "Thermal boundary conductance: A materials science perspective," *Annu. Rev. Mater. Res.* **46**, 433–463 (2016).
- ⁵⁴S. Merabia, S. Shenogin, L. Joly, P. Keblinski, and J.-L. Barrata, "Heat transfer from nanoparticles: A corresponding state analysis," *Proc. Nat. Acad. Sci. U.S.A.* **106**, 15113–15118 (2009).
- ⁵⁵J. C. Duda, C.-Y. P. Yang, B. M. Foley, R. Cheaito, D. L. Medlin, R. E. Jones, and P. E. Hopkins, "Influence of interfacial properties on thermal transport at gold:silicon contacts," *Appl. Phys. Lett.* **102**, 081902 (2013).
- ⁵⁶S. Guenneau, C. Amra, and D. Veynante, "Transformation thermodynamics: Cloaking and concentrating heat flux," *Opt. Express* **20**, 8207–8218 (2012).
- ⁵⁷K. P. Vemuri, F. M. Canbazoglu, and P. R. Bandaru, "Guiding conductive heat flux through thermal metamaterials," *Appl. Phys. Lett.* **105**, 193904 (2014).
- ⁵⁸D. M. Yu, Y. N. Liu, F. L. Tian, X. M. Pan, and X. Q. Sheng, "Accurate thermoplasmonic simulation of metallic nanoparticles," *J. Quant. Spectrosc. Radiat. Transfer* **187**, 150–160 (2017).
- ⁵⁹D. C. Tzarouchis, P. Ylä-Oijala, and A. Sihvola, "Unveiling the scattering behavior of small spheres," *Phys. Rev. B* **94**, 140301 (2016).
- ⁶⁰D. Tzarouchis and A. Sihvola, "Light scattering by a dielectric sphere: Perspectives on the Mie resonances," *Appl. Sci.* **8**, 184 (2018).
- ⁶¹M. Meier and A. Wokaun, "Enhanced fields on large metal particles: Dynamic depolarization," *Opt. Lett.* **8**, 581–583 (1983).
- ⁶²A. Wokaun, J. P. Gordon, and P. F. Liao, "Radiation damping in surface-enhanced Raman scattering," *Phys. Rev. Lett.* **48**, 957–960 (1982).
- ⁶³Here, higher-order terms are required in order to increase the accuracy of the Padé approximate.
- ⁶⁴A. Lalisie *et al.*, *J. Phys. Chem. C* **119**, 25518 (2015).